



1 **Intensive photochemical oxidation in the marine atmosphere:**

2 **Evidence from direct radical measurements**

3 Guoxian Zhang<sup>1,2</sup>, Renzhi Hu<sup>1,\*</sup>, Pinhua Xie<sup>1,2,3,\*\*</sup>, Changjin Hu<sup>1</sup>, Xiaoyan Liu<sup>4</sup>,

4 Liujun Zhong<sup>1</sup>, Haotian Cai<sup>1</sup>, Bo Zhu<sup>5</sup>, Shiyong Xia<sup>5</sup>, Xiaofeng Huang<sup>5</sup>, Xin Li<sup>6</sup>,

5 Wenqing Liu<sup>1</sup>

6 <sup>1</sup>Key Laboratory of Environment Optics and Technology, Anhui Institute of Optics and Fine

7 Mechanics, HFIPS, Chinese Academy of Sciences, Hefei, China

8 <sup>2</sup>University of Science and Technology of China, Hefei, China

9 <sup>3</sup>College of Resources and Environment, University of Chinese Academy of Science, Beijing,

10 China

11 <sup>4</sup>School of Pharmacy, Anhui Medical University, Hefei, China

12 <sup>5</sup>Key Laboratory for Urban Habitat Environmental Science and Technology, School of

13 Environment and Energy, Peking University Shenzhen Graduate School, Shenzhen, China

14 <sup>6</sup>State Key Joint Laboratory of Environmental Simulation and Pollution Control, College of

15 Environmental Sciences and Engineering, Peking University, Beijing, China

16

17 **\*Correspondence to:** Renzhi Hu, Key Laboratory of Environment Optics and

18 Technology, Anhui Institute of Optics and Fine Mechanics, HFIPS, Chinese Academy

19 of Sciences, Hefei, China

20 **\*\*Correspondence to:** Pinhua Xie, University of Science and Technology of China,

21 Hefei, China

22 **Email addresses:** rzhu@aiofm.ac.cn (Renzhi Hu); phxie@aiofm.ac.cn (Pinhua Xie)

23



24 **Abstract:** Comprehensive observations of hydroxyl (OH) and hydroperoxy (HO<sub>2</sub>)  
25 radicals were conducted in October 2019 at a coastal continental site in the Pearl  
26 River Delta (YMK site, 22.55°N, 114.60°E). The average daily maximum OH and  
27 HO<sub>2</sub> concentrations were  $(4.7\text{--}9.5) \times 10^6 \text{ cm}^{-3}$  and  $(4.2\text{--}8.1) \times 10^8 \text{ cm}^{-3}$ , respectively.  
28 The synchronized air mass transport from the northern cities and the South China Sea  
29 exerted a time-varying influence on atmospheric oxidation. Under a typical ocean-  
30 atmosphere (OCM), reasonable measurement model agreement was achieved for both  
31 OH and HO<sub>2</sub> using a 0-D chemical box model incorporating the regional atmospheric  
32 chemistry mechanism version 2-Leuven isoprene mechanism (RACM2-LIM1). Land  
33 mass (LAM) influence promoted more active photochemical processes, with daily  
34 averages of  $7.1 \times 10^6 \text{ cm}^{-3}$  and  $5.2 \times 10^8 \text{ cm}^{-3}$  for OH and HO<sub>2</sub>, respectively.  
35 Intensive photochemistry occurred after precursor accumulation, allowing local net  
36 ozone production comparable with surrounding suburban environments (5.52 ppb/h  
37 during the LAM period). The rapid oxidation process was accompanied by a higher  
38 diurnal nitrous acid (HONO) concentration (> 400 ppt). After a sensitivity test,  
39 HONO-related chemistry elevated the ozone production rate by 33% and 39% during  
40 the LAM and OCM periods, respectively, while the nitric acid and sulfuric acid  
41 formation rates were 52% and 35% higher, respectively. The simulated daytime  
42 HONO and ozone concentrations were reduced to a low level (~70 ppt and ~35 ppb)  
43 without the HONO constraint. This work challenges the conventional recognition of  
44 the MBL in a complex atmosphere. For coastal cities, the particularity of the HONO  
45 chemistry in the MBL tends to influence the ozone-sensitive system and eventually  
46 magnifies the background ozone. Therefore, the promotion of oxidation by elevated  
47 precursor concentrations is worth considering when formulating emission reduction  
48 policies.

49 **Keywords:** FAGE-LIF; OH and HO<sub>2</sub> radicals; Atmospheric oxidation; Marine  
50 boundary layer; Precursors;

51



## 52 **1 Introduction**

53 The marine boundary layer (MBL) occupies 71% of the planetary boundary layer,  
54 is a massive active carbon sink on Earth, and plays an irreplaceable role in coping  
55 with global climate change (Stone et al., 2012; Woodward-Massey et al., 2022b; Liu  
56 et al., 2022a). As a typical background atmosphere on the Earth, the MBL is  
57 equivalent to a natural smog chamber with limited anthropogenic emissions and is  
58 characterized by low NO<sub>x</sub> (the sum of nitric oxide (NO) and nitrogen dioxide (NO<sub>2</sub>))  
59 and non-methane hydrocarbons (NMHCs) under a layer of clean air (Woodward-  
60 Massey et al., 2022b). The lifetime of OH radical, a key oxidant, is on the order of a  
61 few hundred milliseconds (Fuchs et al., 2012). Due to the scarcity of oxidation  
62 precursors, including nitrous acid (HONO), formaldehyde (HCHO), and NMHCs, the  
63 reaction between O<sup>1</sup>D and water vapor generally dominates the radical initiation  
64 pathway in the marine environment. For example, in a tropical boundary layer  
65 observation experiment (reactive halogens in the marine boundary layer, RHaMBLe),  
66 ozone photolysis was found to account for 70% of the OH radical source based on the  
67 master chemical mechanism (MCM) (Whalley et al., 2010). The vital role of ozone  
68 photolysis is contrasting with typical polluted and semi-polluted areas investigated in  
69 a series of field campaigns, in which the propagation routes were found to dominate  
70 the radical source (Yang et al., 2021; Tan et al., 2019a). Therefore, studying the  
71 radical chemistry in the MBL provides a valuable opportunity to test the current  
72 understanding of atmospheric oxidation mechanisms in a natural setting.

73 Since the earliest observations off the coast of northern Norfolk in the Weybourne  
74 Atmospheric Observatory Summer Experiment in June 1995 (WAOSE95), more  
75 observations and simulations of radical chemistry in the MBL environment have been  
76 conducted using ground-based, airborne, and shipborne instruments (Qi et al., 2007;  
77 Kanaya et al., 2002; Kanaya et al., 2001; Mallik et al., 2018; Woodward-Massey et al.,  
78 2022a; Carpenter et al., 2011; Grenfell et al., 1999; Brauers et al., 2001; Whalley et al.,  
79 2010). Most field measurements have yielded well-reproduced OH and HO<sub>2</sub>  
80 concentration profiles via chemical mechanisms, with differences of within ~20%.



81 However, the base model is not sufficient to describe the radical chemistry in some  
82 exceptional cases, especially in regard to the HO<sub>2</sub> radical. Considering the practical  
83 association between halogen (Cl, Br, and I) chemistry and heterogeneous chemistry in  
84 marine new particle formation, particularly the involvement of heterogeneous iodine-  
85 organic chemistry, exploring the synchronous influence of these mechanisms on HOx  
86 (OH and HO<sub>2</sub>) radical chemistry in the MBL region is a worthy endeavor (Xu et al.,  
87 2022; Huang et al., 2022). The mixing of air masses of continental and marine origins  
88 can lead to more variability in radical concentrations. During seasonal measurements  
89 of both OH and HO<sub>2</sub> in the Atlantic Ocean, variance analysis indicated that around 70%  
90 of the variance of OH and HO<sub>2</sub> was due to diurnal behavior (in the form of photolysis  
91 frequency), while the remaining variance was attributed to long-term seasonal cycles  
92 (in the form of the changes in O<sub>3</sub>, CO and air mass contribution) (Vaughan et al.,  
93 2012).

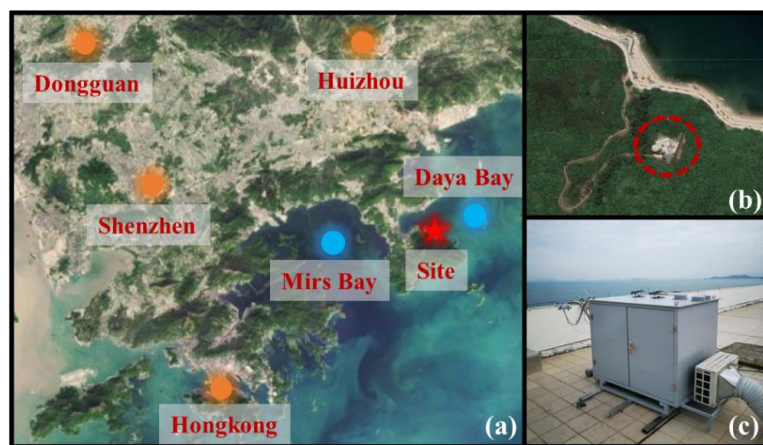
94 The Chinese economy has undergone rapid development in recent years, and the  
95 co-occurrence of primary and secondary regional pollution has become a severe  
96 problem (Lu et al., 2019; Liu et al., 2022c). The interactions between air pollutants  
97 from upwind cities, shipping vessels, and other anthropogenic emissions lead to  
98 precursor accumulation (Sun et al., 2020; Zeren et al., 2022). The background ozone  
99 concentration in key regions of China has increased year by year, highlighting the  
100 significant influence of anthropogenic activities on the atmospheric oxidation in  
101 background regions in China (Wang et al., 2009; Chen et al., 2022). However, little  
102 research has been dedicated to the radical chemistry and oxidation mechanism in  
103 regions with both coastal and continental features. To fill this research gap, in this  
104 study, a field campaign was conducted on photochemistry in the MBL at a coastal site  
105 in the Pearl River Delta. The OH and HO<sub>2</sub> radicals associated with other related  
106 species were measured in October 2019, and the radical-related oxidation process was  
107 identified to determine the photochemical efficiency in the marine atmosphere.

## 108 **2 Materials and methods**



## 109 2.1 Site description

110 As shown in Fig. 1(a), this observation campaign lasted for 11 days from  
111 October 18 to October 28, 2019, in Yangmeikeng (YMK, 22.55°N, 114.60°E), a  
112 coastal site in Shenzhen, Pearl River Delta. As the core city of the Greater Bay Area,  
113 Shenzhen is bordered by Dongguan to the north, Huizhou to the east, and Hong Kong  
114 to the south. The YMK site is on the Dapeng Peninsula, to the southeast of Shenzhen,  
115 between Mirs Bay and Daya Bay. As it is adjacent to the port of Hong Kong,  
116 precursors from ship emissions may influence the atmospheric chemistry. The site is  
117 approximately 35 m above sea level, and the sea is approximately 150 m to the east.  
118 No apparent local emissions exist, and the surrounding forest is lush (Fig. 1(b)). In  
119 addition to anthropogenic and vegetation emissions, the site is also affected by the  
120 synchronization of plumes from northern cities and the South China Sea (Niu et al.,  
121 2022; Xia et al., 2021). Due to its significant time-varying pollution characteristics,  
122 this area is an ideal site for studying the effects of plume transport on atmospheric  
123 oxidation.



124  
125 **Fig. 1.** Details of the observation site (a) The location of the measurement site and surrounding cities. The satellite  
126 map data is extracted from © Google Earth. (b) The close shot of the measurement site location. (c) The actual image  
127 for the LIF-Box.

## 128 2.2 Instrumentation

### 129 2.2.1 HO<sub>x</sub> radical measurements

130 The OH and HO<sub>2</sub> radicals were measured via laser-induced fluorescence (LIF).



131 The OH radical can be directly measured by exciting the fluorescence using a 308-nm  
132 laser. HO<sub>2</sub> is converted into the OH radical via chemical transformation and then  
133 detected in the form of OH radical. The self-developed instrument, the Anhui Institute  
134 of Optics Fine Mechanics-LIF (AIOFM-LIF), was used to conduct the measurements  
135 (Zhang et al., 2022a; Wang et al., 2021; Wang et al., 2019). This system has been used  
136 in key regions of China, including the Yangtze River Delta, Pearl River Delta, and  
137 Chengdu-Chongqing region, and achieved good performance in a comparison  
138 experiment with a LIF system jointly developed by Forschungszentrum Jülich and  
139 Peking University (PKU-LIF) (Zhang et al., 2022b).

140 The system and detection interference process have been described in detail in  
141 previous studies (Zhang et al., 2022a). Briefly, the system consists of a laser output  
142 module, a radical detection module, and a control and data acquisition module. These  
143 modules are integrated into a sampling box with constant temperature and humidity  
144 control (Fig. 1(c)). The laser output module is a union of an Nd:yttrium-aluminum-  
145 garnet (YAG) solid-state laser, a 532-nm laser output, and a tunable dye laser. In the  
146 radical detection module, the OH and HO<sub>2</sub> fluorescence cells are combined in parallel  
147 and share a common axial optical path. The 308-nm laser is introduced into the HO<sub>2</sub>  
148 cell first and then into the OH cell via an 8-m fiber. To maintain the detection  
149 efficiency, the power in the OH fluorescence cell should be at least 15 mW. In the  
150 detection process, a set of lenses was deployed and positioned in front of the  
151 microchannel plate detector (MCP) to boost the fluorescence collection capacity. Each  
152 MCP detector contains a timing control instrument to optimize the signal-to-noise  
153 ratio (SNR) of the fluorescence detection. Efficient ambient air sampling was  
154 achieved using an aluminum nozzle (0.4 mm orifice), and the pressure in the chamber  
155 was maintained at 400 Pa via a vortex vacuum pump (XDS35i, Edwards) to avoid  
156 fluorescence quenching.

157 A wavelength modulation for the background measurement that periodically  
158 switches from an on-resonant state to a non-resonant state has been widely used to  
159 obtain spectral zero. The ozone photolysis interference was subtracted according to



160 laboratory experiments. An OH measurement comparison with an interference-free  
161 instrument, PKU-LIF, was conducted in a real atmosphere in a previous study (Zhang  
162 et al., 2022b). The ozonolysis interference on the measurement consistency of both  
163 systems was excluded under high-NO<sub>x</sub> and high-NMHC conditions, confirming the  
164 general applicability under complex atmospheric pollution. For HO<sub>2</sub> measurement,  
165 the NO concentration corresponding to a conversion efficiency of ~15% was selected  
166 to avoid RO<sub>2</sub>→HO<sub>2</sub> interference (especially from RO<sub>2</sub> radicals derived from long-  
167 chain alkanes (C ≥ 3), alkenes, and aromatic hydrocarbons).

168 A standard HO<sub>x</sub> radical source based on the simultaneous photolysis of H<sub>2</sub>O/O<sub>2</sub>  
169 by a 185 nm mercury lamp was used to complete the calibration of the detection  
170 sensitivity (Wang et al., 2020). During the observation campaign, the instrument was  
171 calibrated every 1 or 2 days (except for shutdown during rainy periods), and the  
172 sensitivity used for the data processing was an average of all of the calibration results.  
173 Considering the system error and calibration error, the detection limits of the OH and  
174 HO<sub>2</sub> radicals were  $3.3 \times 10^5 \text{ cm}^{-3}$  and  $1.1 \times 10^6 \text{ cm}^{-3}$  (60 s, 1σ), respectively, at a  
175 typical laser power of 15 mW, and the measurement errors were 13% and 17%,  
176 respectively.

### 177 **2.2.2 Supporting measurements**

178 In addition to measuring the HO<sub>x</sub> radicals, an extensive suite of relevant species  
179 was also measured close to the LIF instrument to improve the analysis of the radical  
180 photochemistry. Detailed information about the measurement instrument is presented  
181 in Table S1, including the meteorological parameters (wind speed (WS), wind  
182 direction (WD), temperature (T), relative humidity (RH), pressure (P), and solar  
183 radiation (J-values)), conventional pollutants (ozone (O<sub>3</sub>), carbonic oxide (CO), and  
184 sulfur dioxide (SO<sub>2</sub>)), secondary pollution precursors (HONO, NO, NO<sub>2</sub>, HCHO, and  
185 NMHCs), and destruction products (particulate matter (PM<sub>2.5</sub>)). In addition to HCHO,  
186 other volatile organic compounds (VOCs) were detected using a gas chromatograph  
187 coupled with a flame ionization detector and mass spectrometer (GC-FID-MS).  
188 Ninety-nine types of VOCs, including C<sub>2</sub>–C<sub>11</sub> alkanes, C<sub>2</sub>–C<sub>6</sub> alkenes, C<sub>6</sub>–C<sub>10</sub>



189 aromatics, halohydrocarbons, and some oxygenated VOCs (OVOCs), were observed  
190 using the GC-FID-MS at a 1-h time interval. Only isoprene was considered as a  
191 representative of biogenic VOCs (BVOCs). All of the instruments were located close  
192 to the roof of the fourth floor, nearly 12 m above the ground to ensure that all of the  
193 pollutants were located in a homogeneous air mass.

### 194 **2.3 Model description**

195 A 0-D chemical box model incorporating a condensed mechanism, the regional  
196 atmospheric chemistry mechanism version 2-Leuven isoprene mechanism (RACM2-  
197 LIM1), was used to simulate the radical concentrations and the generation of radical-  
198 related secondary pollution (Stockwell et al., 1997; Griffith et al., 2013; Tan et al.,  
199 2017). The meteorological parameters, conventional pollutants, and precursor  
200 concentrations mentioned in Section 2.2.2 were input into the model as boundary  
201 conditions. All of the constraints were unified to a temporal resolution of 15 min  
202 through averaging or linear interpolation. The overall average during the observations  
203 was substituted for large areas of missing data due to instrument maintenance or  
204 failure. Three days of data were entered in advance as the spin-up period, and a  
205 synchronized time-dependent dataset was eventually generated. The hydrogen (H<sub>2</sub>)  
206 and methane (CH<sub>4</sub>) concentrations were set to fixed values of 550 ppb and 1900 ppb,  
207 respectively. The physical losses of species due to processes such as deposition,  
208 convection, and advection were approximately replaced by an 18 h atmospheric  
209 lifetime. According to the measurement accuracy, the simulation accuracy of the  
210 model for the OH and HO<sub>2</sub> radicals was 50% (Zhang et al., 2022a).

211 Considering the environmental characteristics of the MBL, the gas-phase  
212 mechanisms for bromine (Br<sub>2</sub>) were introduced into the base model to diagnose the  
213 impacts of the reactive bromine chemistry at the field site. The details of the  
214 mechanisms involved are listed in Tables S2 and S3. The halogen species were not  
215 available in the YMK site, so the Br<sub>2</sub> concentration during the same season at a  
216 coastal site in the Pearl River Delta was used as a reference value (average daytime  
217 concentration of 3–5 ppt at a coastal ground site in Hong Kong, China).





## 218 **3 Results**

### 219 **3.1 Meteorological and chemical parameters**

#### 220 **3.1.1 Data overview**

221 Fig. S1 presents the time series of the main meteorological parameters and  
222 pollutants during the observation period at the YMK site. Except for on 2 days,  
223 October 26 and 28, the meteorological characteristics of the other days were generally  
224 stable. The daily maximum T, RH, and J-values did not vary significantly. The  
225 suitable temperature (20–30°C) and humidity (50–80%) conditions promoted the  
226 stable oxidation of the diurnal photochemistry. The peak  $j(\text{O}^1\text{D})$  value was  
227 approximately  $2.0 \times 10^{-5} \text{ s}^{-1}$ , exhibiting the typical characteristics of intense light  
228 radiation in autumn in the Pearl River Delta region (Yang et al., 2022a; Tan et al.,  
229 2022).

230 As typical marine air components, the concentrations of NO<sub>x</sub>, CO, PM<sub>2.5</sub>, and  
231 other pollutants were lower than those detected in other observation campaigns in  
232 both urban and suburban areas in the Pearl River Delta region (Tan et al., 2019b; Lu et  
233 al., 2012; Yang et al., 2022b). The PM<sub>2.5</sub> and CO concentrations exhibited good  
234 consistency and even mild pollution features on some dates, reflecting the influence  
235 of human activities. Contrary to the conventional belief that marine ozone is a global  
236 background setting, the ozone concentration in the YMK site was always at the  
237 critical value of the updated Class I standard (GB3095-2012, average hourly O<sub>3</sub> of 81  
238 ppb at 25°C and 1013 kPa). The occurrence of fewer emissions reduced the titration  
239 effect, resulting in the ozone exhibiting no apparent diurnal trend on some of the dates  
240 and a high background value at night ( $67.3 \pm 7.6$  ppb). The NO<sub>x</sub> concentrations also  
241 maintained typically low levels on most dates. The daily maximum NMHC  
242 concentration peaked at  $19.3 \pm 3.0$  ppb, and the maximum value of ~40 ppb occurred  
243 on October 27. Local biological emissions significantly affected the NMHC  
244 composition of the site, and isoprene, a representative BVOC, achieved a noon  
245 maximum of  $0.82 \pm 0.16$  ppb. Neither anthropogenic alkenes nor aromatic



246 hydrocarbons were abundant, and OVOCs accounted for approximately 50% of the  
 247 total. As a photochemical indicator, formaldehyde peaked at ~4 to ~8 ppb on October  
 248 18, 19, and 27, suggesting a more vigorous oxidation process. HONO exhibited a  
 249 grooved distribution with high daytime ( $0.49 \pm 0.097$  ppb) and low nighttime ( $0.20 \pm$   
 250  $0.11$  ppb) concentrations. This unique distribution of HONO has been observed in  
 251 remote environments in several previous observation campaigns (Jiang et al., 2022;  
 252 Crilley et al., 2021). An extremely high daytime HONO concentration will  
 253 significantly affect the chemical composition of the atmosphere and the secondary  
 254 pollution generation.

255 **Table 1.** Summary of radical concentrations and related species concentrations at MBL. All data are listed as the  
 256 average in noontime (10:00–15:00).

| Campaign            | Location                      | Date               | OH<br>( $10^6\text{cm}^{-3}$ ) | HO <sub>2</sub><br>( $10^8\text{cm}^{-3}$ ) | HCHO<br>(ppb) | HONO<br>(ppb) | NO <sub>x</sub><br>(ppb) | O <sub>3</sub><br>(ppb) | Ref                                |
|---------------------|-------------------------------|--------------------|--------------------------------|---|---------------|---------------|--------------------------|-------------------------|------------------------------------|
| WAOSE95             | Weybourne, UK                 | 1995<br>(Jun)      | 5.0                            | -   | 1.50          | 0.10          | <2.0                     | 40.0                    | (Grenfell et al., 1999)            |
| ALBATROSS           | Atlantic Ocean                | 1996<br>(Oct-Nov)  | 7.0                            | -   | 0.50          | -             | -                        | 25.0                    | (Brauers et al., 2001)             |
| EASE96              | Mace Head,<br>Ireland         | 1996<br>(Jul-Aug)  | 2.3                            | 2.6   | -             | -             | ~1.0                     | 45.0                    | (Carslaw et al., 1999)             |
| EASE97              | Mace Head,<br>Ireland         | 1997<br>(Apr-May)  | 1.8                            | 1.0   | 0.70          | -             | 0.95                     | 46.0                    | (Creasey et al., 2002)             |
| ORION99             | Okinawa Island,<br>Japan      | 1999<br>(Aug)      | 4.0                            | 4.3   | -             | 0.20          | 6.3                      | 23.0                    | (Kanaya et al., 2001)              |
| RISOTTO             | Rishiri Island,<br>Japan      | 2000<br>(June)     | 7.4                            | 3.1   | -             | -             | 0.45                     | -                       | (Kanaya et al., 2002)              |
| RISFEX              | Rishiri Island,<br>Japan      | 2003<br>(Aug)      | 2.7                            | 1.5   | -             | -             | 0.2                      | 28.0                    | (Qi et al., 2007)                  |
| RHaMBLe             | Cape Verde,<br>Atlantic Ocean | 2007<br>(May-Jun)  | 9.0                            | 6.0   | 0.30          | -             | 0.014                    | 35.0                    | (Whalley et al., 2010)             |
| SOS                 | Cape Verde,<br>Atlantic Ocean | 2009<br>(Jun; Sep) | 9.0                            | 4.0   | 1.9           | -             | 0.050                    | 40.0                    | (Carpenter et al., 2011)           |
| CYPHEX              | Cyprus,<br>Mediterranean      | 2014<br>(Jul)      | 5.8                            | 6.3   | ~1.0          | ~0.080        | <1.0                     | 69.0                    | (Mallik et al., 2018)              |
| ICOZA<br>(NW-SE)    | North Norfolk,<br>UK          | 2015<br>(Jul)      | 3.0                            | 1.4   | 0.9           | 0.052         | 2.0                      | 39.0                    | (Woodward-Massey et al.,<br>2022b) |
| ICOZA<br>(SW)       | North Norfolk,<br>UK          | 2015<br>(Jul)      | 4.1                            | 1.0   | 1.1           | 0.097         | 3.0                      | 31.0                    | (Woodward-Massey et al.,<br>2022b) |
| HT                  | Hok Tsui,<br>China            | 2020<br>(Oct-Nov)  | 4.9                            | -   | 1.0           | 0.15          | ~4.0                     | 65.0                    | (Zou et al., 2022)                 |
| YMK<br>(Land Mass)  | Shenzhen,<br>China            | 2019<br>(Oct)      | 7.1                            | 5.2   | 3.4           | 0.66          | 6.4                      | 75.6                    | This work                          |
| YMK<br>(Ocean Mass) | Shenzhen,<br>China            | 2019<br>(Oct)      | 4.5                            | 4.9   | 1.2           | 0.48          | 3.0                      | 78.1                    | This work                          |

257

### 258 3.1.2 Influences of different air masses

259 During the YMK observation campaign, the wind direction was mainly easterly

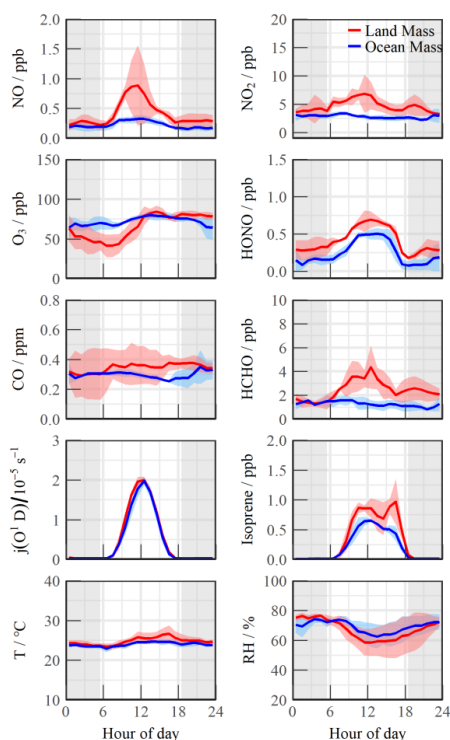


260 and southerly, and the wind speed was below 3 m/s. The conventional wind direction  
261 is insufficient to reflect the air mass trajectory at a slightly higher altitude due to the  
262 mountain-valley breeze (Niu et al., 2022). Using the hybrid single-particle Lagrangian  
263 integrated trajectory (HYSPLIT) model, the 24-h backward trajectories on special  
264 days were obtained (Fig. S2). In Fig. S2, the red, blue, and green trajectories represent  
265 the results at altitudes of 100, 500, and 1000 m above ground level, respectively. Two  
266 typical transportation pathways dominated the air parcels. One originated from the  
267 northern megacities in the Pearl River Delta (defined as the land mass, LAM),  
268 especially on October 18, 19, and 27. In contrast, a clean air mass from the east or  
269 northeast was mainly transported to the observation site from the ocean (defined as  
270 the ocean mass, OCM), with representative episodes on October 22, 25, and 26.

271 Serval observation campaigns have discovered the relationship between wind  
272 direction and radical chemistry (Lu et al., 2012; Fuchs et al., 2017; Niu et al., 2022).  
273 Although there was no apparent wind speed condition, the dominant air mass still  
274 influenced the pollutant concentrations due to the particularity of the marine site.  
275 During the OCM period, the NO<sub>x</sub> and HCHO concentrations exhibited relatively  
276 clean characteristics that were consistent with those previously reported (Table 1).  
277 However, both the HONO and O<sub>3</sub> concentrations were twice as high as those of the  
278 other components, and their daily average values (10:00–15:00) reached 0.48 ppb and  
279 78.1 ppb, respectively. Compared with the OCM period, the meteorological  
280 conditions (T, RH, and J-values) changed greatly during the LAM episode. The  
281 pollutants were accumulated due to the transport of the plume from the northern cities  
282 (Fig. 2). Both NO and NO<sub>2</sub> peaked at around 10:00, exhibiting prominent pollution  
283 characteristics. The diurnal peaks of the HONO and HCHO concentrations were much  
284 higher than those of the Integrated Chemistry of Ozone in the Atmosphere (ICOZA)  
285 Project observations (a pollution period dominated by a southwest wind direction)  
286 (Woodward-Massey et al., 2022b). The HONO concentration was 6.8 times higher  
287 than when the wind direction was southwest in the ICOZA observations, while the  
288 HCHO concentration was 3.1 times higher. The abundance of oxidation precursors



289 (HONO, HCHO, O<sub>3</sub>, and NMHCs) reflected the unique atmospheric conditions in the  
 290 marine environment in China, which originated from the complex atmospheric  
 291 pollution.



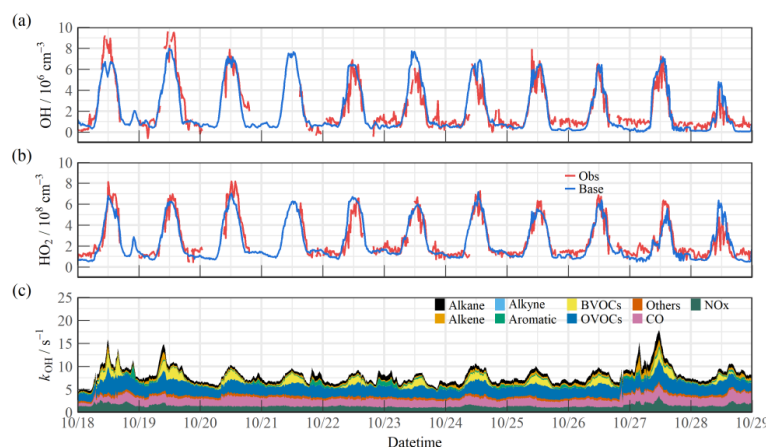
292  
 293 **Fig. 2.** Mean diurnal profiles of measured trace gases parameters during Land mass and Ocean mass episodes. The  
 294 coloured shadows denote the 25 and 75% percentiles. The grey areas denote nighttime.

### 295 **3.2 HO<sub>x</sub> radical concentrations and modeled OH reactivity**

296 Fig. 3(a) and (b) shows the time series of the simulated and observed OH and  
 297 HO<sub>2</sub> radical concentrations during the observation campaign. The time series of the  
 298 simulated OH reactivity ( $k_{OH}$ ) is presented in Fig. 3(c). The observed OH and HO<sub>2</sub>  
 299 radicals exhibited significant diurnal trends. The average daily maximum OH and  
 300 HO<sub>2</sub> values were  $(4.7\text{--}9.5) \times 10^6 \text{ cm}^{-3}$  and  $(4.2\text{--}8.1) \times 10^8 \text{ cm}^{-3}$ , respectively. The  
 301 peak  $k_{OH}$  value was commonly less than  $10 \text{ s}^{-1}$ . Due to human activities, the simulated  
 302  $k_{OH}$  reached more than  $\sim 15 \text{ s}^{-1}$  on some days. The radical concentrations and  
 303 reactivity exhibited similar trends, which differed from reports on urban and semi-  
 304 urban areas where inorganic species (NO<sub>x</sub> and CO) were the dominant controllers of



305  $k_{OH}$  (Zhang et al., 2022a; Tan et al., 2019b; Lou et al., 2010).

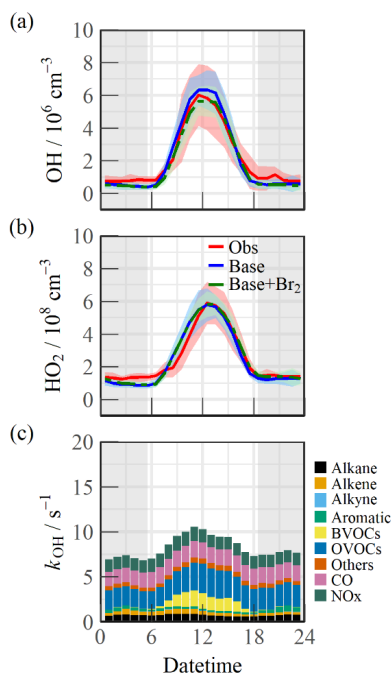


306  
307 **Fig. 3.** Timeseries of the observed and modelled parameters for OH, HO<sub>2</sub> and  $k_{OH}$  during the observation  
308 period. (a) OH, (b) HO<sub>2</sub>, (c)  $k_{OH}$ .

309 The OH and HO<sub>2</sub> concentrations were calculated using a base model  
310 incorporating the RACM2-LIM1 mechanism. Overall, the observed OH and HO<sub>2</sub>  
311 concentration data were both well reproduced by the base model (Fig. 4(a)–(b)). The  
312 base model slightly overestimated the OH radical, suggesting that a radical removal  
313 pathway was missing. Halogen species have been recognized as potent oxidizers that  
314 can boost photochemistry (Xia et al., 2022; Peng et al., 2021). A sensitivity test was  
315 performed by imposing ~3 ppt Br<sub>2</sub>, a typical mixing ratio reported for a coastal site in  
316 the Pearl River Delta, into the base model to diagnose the impact of the halogen  
317 chemistry on the troposphere chemistry (Xia et al., 2022). The details of the  
318 mechanisms involved are listed in Tables S2 and S3. In this scenario (Fig. 4(a)–(b),  
319 green line), the simulated OH was 11.6% lower than in the base model, and no  
320 significant effect on the HO<sub>2</sub> radical was identified. The daily maximum calculated  
321 total OH reactivity was 9.9 s<sup>-1</sup> (Fig. 4(c)). Regarding the contributions of the  
322 inorganic species, the contributions of CO and NO<sub>x</sub> were close at 18.0% and 14.8%,  
323 respectively. Nearly 70% of the reactivity was accounted for by the organic species,  
324 among which the OVOCs were the largest contributor (30.6%). The anthropogenic  
325 alkanes, alkenes, and aromatic hydrocarbons contributed less than 10% to the  
326 reactivity in the marine environment. The BVOCs emitted by the surrounding forest



327 could not be ignored, accounting for 15.7%.



328

329

330

**Fig. 4.** Median diurnal profiles of the observed and modelled parameters for OH, HO<sub>2</sub> and  $k_{\text{OH}}$  during the observation period. (a) OH, (b) HO<sub>2</sub>, (c)  $k_{\text{OH}}$ .

331

332

333

334

335

336

337

338

339

340

341

342

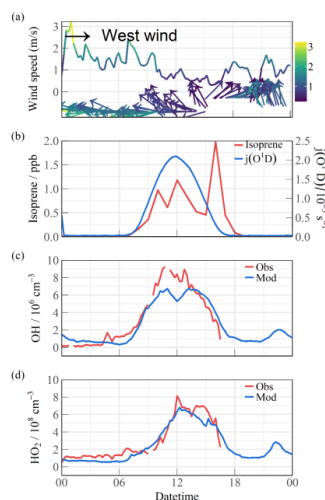
343

344

The regional transport of radicals was generally impossible due to their short lifetimes. However, the air mass transport of the precursors increase the RO<sub>x</sub> primary sources. Under the linkage of NO concentration, this leads to accelerated cycling efficiency of the radicals, promoting the accumulation of photochemical products. The effects can be seen directly in the changes to the oxidation level. Isoprene is discussed as an example. The prevailing wind direction experienced a series of southerly-easterly shifts from 8:00 to 18:00 on October 18 (Fig. 5(a)). The growth and decline of the isoprene concentration were highly correlated with the changes in the wind direction (Fig. 5(b)), and the maximum concentration (2.1 ppb) occurred at 17:00 under the southwest wind. Correspondingly, the sensitive LIF instrument captured the decrease in the concentration at noon. The base model simulated the fluctuations in the OH concentration, but the solar radiation did not vary, indicating that the change in the precursor accelerated the instantaneous OH → HO<sub>2</sub> propagation (Fig. 5(c)). In addition, the evolution of the air mass composition inhibited the



345 conversion of HO<sub>2</sub> to OH and maintained the high HO<sub>2</sub> level during the afternoon  
 346 (Fig. 5(d)).

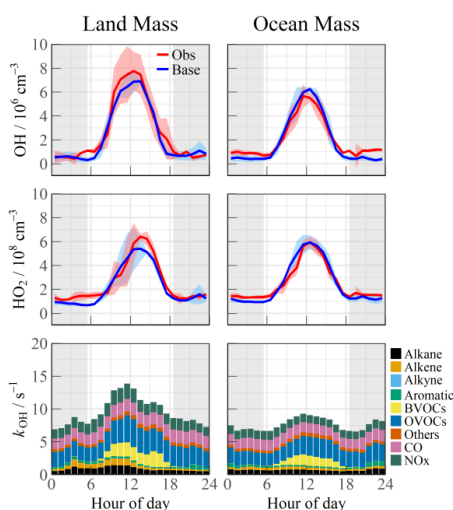


347 **Fig. 5.** Median diurnal profiles of the observed and modelled parameters during a typical case of rapid wind  
 348 direction change on October 18. (a) Wind direction and speed, (b) Isoprene concentration and solar radiation  
 349 (j(O'D)), (c) The observed and modelled OH concentration, (d) The observed and modelled HO<sub>2</sub> concentration.

351 Therefore, it is worth comparing the concentrations and reactivities of the radicals  
 352 by classifying the predominant air mass (Fig. 6). During the OCM period, the  
 353 observed OH and HO<sub>2</sub> radicals could be reflected by the base chemical mechanism,  
 354 with daily averages of  $4.5 \times 10^6 \text{ cm}^{-3}$  and  $4.9 \times 10^8 \text{ cm}^{-3}$ , respectively. Compared to  
 355 other campaigns (Table 1), the observed maximum values were within reasonable  
 356 ranges (OH:  $2\text{--}9 \times 10^6 \text{ cm}^{-3}$ ; HO<sub>2</sub>:  $1\text{--}6 \times 10^8 \text{ cm}^{-3}$ ). Despite low NO<sub>x</sub> levels during  
 357 the OCM period, the HO<sub>2</sub> radical was not overestimated using the base model, which  
 358 was dissimilar to many MBL observations. The heterogeneous uptake pathway did not  
 359 need to be further investigated due to the low PM<sub>2.5</sub> concentration during the OCM  
 360 period ( $< 25 \mu\text{g}/\text{m}^3$ ). However, both the OH and HO<sub>2</sub> radical concentrations reached  
 361 higher levels during the LAM-dominant period, indicating a more active  
 362 photochemical process. The diel averages for the OH and HO<sub>2</sub> radicals were  $7.1 \times 10^6$   
 363  $\text{cm}^{-3}$  and  $5.2 \times 10^8 \text{ cm}^{-3}$ , respectively, which were notably higher than the levels  
 364 reported in the ICOZA observations (Woodward-Massey et al., 2022b). The base  
 365 model underestimated both the OH and HO<sub>2</sub> concentrations between 10:00 and 15:00,  
 366 and the observation-to-model ratio was greater than 1.2. Compared with the OCM-



367 dominant episode, the higher reactivity during the LAM period indicated the  
 368 occurrence of efficient recycling during the ROx propagation ( $12.4 \text{ s}^{-1}$  vs.  $8.8 \text{ s}^{-1}$ ).  
 369 The higher contributions of the BVOCs (only isoprene was considered, 15.6%) and  
 370 OVOCs (30.2%) to the reactivity reflected the diverse composition of the VOCs in the  
 371 forest environment. The more reactive atmosphere did not introduce a missing OH  
 372 source in the afternoon, but radical cycling under enhanced photochemistry is worth  
 373 discussing (Hofzumahaus et al., 2009). As a representative of the OVOCs, HCHO  
 374 reflects the photochemical level to a certain extent. As shown in Fig. S3, a solid  
 375 positive dependence between the  $\text{OH}_{\text{obs-to-OH}_{\text{mod}}$  ratio and HCHO was observed (the  
 376 daytime data were restricted according to  $j(\text{O}^1\text{D}) > 5 \times 10^{-6} \text{ s}^{-1}$ ). Considering the  
 377 essential contributions of the OVOCs and BVOCs during ROx recycling, the other  
 378 unmeasured species (mono-terpenes and reactive halogens) involved in the oxidation  
 379 cycle were responsible for the elevated photochemistry. Obtaining the full magnitude  
 380 of the radical-related parameters is necessary to compensate for the discrepancy in the  
 381 concentration closure experiments.



382  
 383  
 384  
 385

**Fig. 6.** Median diurnal profiles of the observed and modelled OH, HO<sub>2</sub>, k<sub>OH</sub> during LAM and OCM episodes. The coloured shadows for OH and HO<sub>2</sub> radicals denote the 25 and 75% percentiles. The grey areas denote nighttime.

## 386 4 Discussion

### 387 4.1 Experimental radical budget balance





#### 388 4.1.1 OH radical

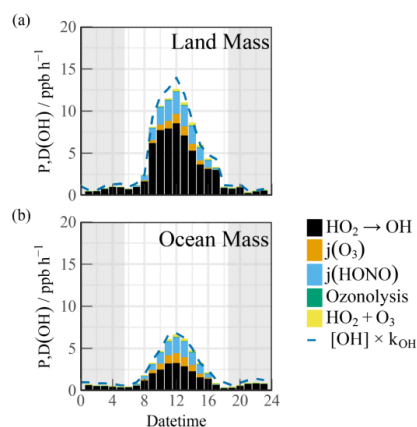
389 A process-oriented experiment was conducted to investigate the photochemistry  
390 progress from a budget balance perspective (Woodward-Massey et al., 2022a; Tan et  
391 al., 2019b; Yang et al., 2021). The OH was in a photostationary steady state due to its  
392 short lifetime. The total OH removal rate was directly quantified from the union of the  
393 OH concentration and the reactivity (R (1)):

$$394 \quad D(OH) = [OH] \times k_{OH}. \quad (1)$$

395 The total production rate of the OH radical was the sum of the primary sources  
396 ( $O_3$ /HONO photolysis and ozonolysis reactions) and secondary sources ( $HO_2 + NO$ )  
397 (R (2)):

$$398 \quad P(OH) = j_{HONO}[HONO] + \varphi_{OH} j(O^1D)[O_3] + \Sigma i \{ \varphi_{OH}^i k_{Alkenes+O_3}^i [Alkenes][O_3] \}$$
$$399 \quad + (k_{HO_2+NO}[NO] + k_{HO_2+O_3}[O_3])[HO_2]. \quad (2)$$

400 The diel profiles of the experimental OH budget during the LAM and OCM  
401 periods are shown in Fig. 7. Both the observed OH and  $HO_2$  radicals were introduced  
402 into the budget calculations. Because  $k_{OH}$  was not measured during the observation  
403 experiment, the simulated value was used as the lower limit to analyze the removal  
404 rate (Yang et al., 2022b). During the OCM period, the  $HO_2 + NO$  reaction accounted  
405 for ~50% of the OH yield. The maximum of 6.6 ppb/h occurred at around 12:00. The  
406 photolysis reactions could increase the daytime contributions of HONO and  $O_3$  to  
407 1.52 ppb/h and 0.84 ppb/h, respectively (10:00–15:00). The contribution of the non-  
408 photolytic radical source (ozonolysis reactions) was almost negligible.



409  
410  
411

Fig. 7. The diurnal profiles of the experimental OH budget during (a) Land mass and (b) Ocean mass episodes. The blue line denotes the OH destruction rate ( $[OH] \times k_{OH}$ ). The grey areas denote nighttime.

412

413

414

415

416

417

418

419

420

421

422

423

Compared with other marine observations, the calculated OH generation rate was approximately twice that reported in the ICOZA Project and five times that obtained in the RHaMBLe Project (Woodward-Massey et al., 2022a; Whalley et al., 2010). During the LAM period, the OH generation rate reached a maximum of 12.6 ppb/h, accompanied by a secondary source contribution of 67% (from the reaction between HO<sub>2</sub> and NO) during the daytime, which was close to several observations related to polluted plumes (Woodward-Massey et al., 2022a; Tan et al., 2019b; Lu et al., 2012; Yang et al., 2022b). No additional OH radical source was needed when the simulated  $k_{OH}$  was introduced into the experimental budgets. The difference between P(OH) and D(OH) was less than 2 ppb/h, indicating the absence of a nontraditional OH recycling pathway (X mechanism) under low NO concentration conditions (Hofzumahaus et al., 2009).

424

#### 4.1.2 Total ROx radicals

425

426

427

428

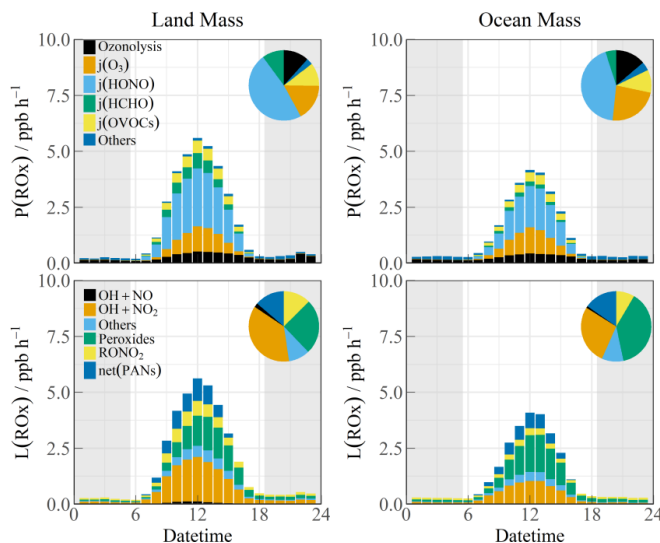
429

430

The budget analysis of the HO<sub>2</sub> and RO<sub>2</sub> radicals could not be performed well due to the lack of RO<sub>2</sub> radical observation data. The diurnal profiles of the ROx production (P(ROx)) and termination rate (L(ROx)) for the different air masses are shown in Fig. 8. The P(ROx) could reach 3.36 ppb/h with an ocean plume. HONO photolysis controlled nearly half of the primary sources (45.7%), and the daily distribution was consistent with that of solar radiation. The ozone-related



431 contributions from photolysis and ozonolysis were approximately 25.1% + 11.5%.  
 432 The remaining contribution was from the photolysis of carbonyls (HCHO and  
 433 OVOCs) (15.0%). The anthropogenic contribution to the radical chemistry was not  
 434 ignorable, and the ROx source in this observation was exponentially higher than that  
 435 in other MBL observations (Woodward-Massey et al., 2022a; Stone et al., 2012;  
 436 Whalley et al., 2010; Mallik et al., 2018). The P(ROx) of the LAM was close to that  
 437 in Shenzhen (~4 ppb/h) but was significantly lower than that in Yufa (~7 ppb/h) and  
 438 the BackGarden (~11 ppb/h) (Tan et al., 2019b; Lu et al., 2012; Yang et al., 2022b).  
 439 The reactions between ROx and NOx and self-combination were the main pathways  
 440 of radical termination (~70%). The contribution of the formation of peroxyxynitrite to  
 441 the L(ROx) could not be ignored in the daytime.



442  
 443 **Fig. 8.** The diurnal profiles of ROx budget during Land mass and Ocean mass episodes. The pie chart denotes  
 444 proportions in different parts during the daytime (10:00-15:00). The grey areas denote nighttime.

445 Due to the high HONO concentration during the daytime, the photolysis reaction  
 446 made daytime contributions of 1.52 ppb/h and 2.19 ppb/h during the OCM and LAM  
 447 periods, respectively. As the only known gas-phase source, OH + NO accounted for a  
 448 negligible proportion of the HONO loss. Considering the location of the YMK site,  
 449 HONO from cruise ship emissions is a possible component of the primary  
 450 anthropogenic source (Sun et al., 2020). Other active tropospheric HONO sources



451 (heterogeneous reactions with  $\text{NO}_2$  and  $p(\text{NO}_3^-)$  photolysis) are worthy of  
452 consideration and significantly contribute to the atmospheric oxidation in the MBL  
453 area (Zhu et al., 2022; Crilley et al., 2021).

#### 454 **4.2 Local ozone production rate**

455 Peroxyl radical chemistry is the essential photochemical source of tropospheric  
456 ozone (F(Ox), R (3)):

$$457 \quad F(O_x) = k_{\text{HO}_2+\text{NO}}[\text{NO}][\text{HO}_2] + \sum_i k_{\text{RO}_2^i+\text{NO}}[\text{NO}]\text{RO}_2^i. \quad (3)$$

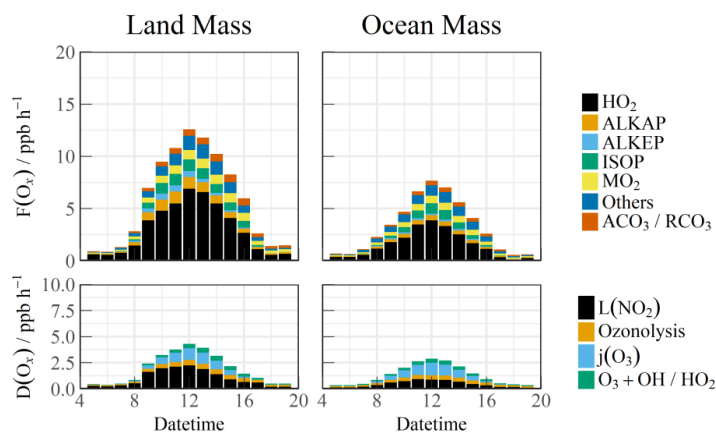
458 NO reacts with  $\text{HO}_2$  and  $\text{RO}_2$  radicals to form  $\text{NO}_2$ , and then, photolysis occurs to  
459 form  $\text{O}_3$  under solar radiation.  $\text{NO}_2$  and ozone are the two sides of the oxidation  
460 reservoir. The effect of local emissions on the photodynamic equilibrium can be  
461 avoided by characterizing the photochemical production of the total oxidants (Tan et  
462 al., 2019b). Ox is mainly photochemically removed through ozone photolysis,  
463 ozonolysis, radical chain propagation ( $\text{OH}/\text{HO}_2 + \text{O}_3$ ), and chain termination ( $\text{OH} +$   
464  $\text{NO}_2$ ) reactions in the troposphere (D(Ox), R (4)):

$$465 \quad D(O_x) = \varphi_{\text{OH}}(O^1D)[\text{O}_3] + \sum_i \{k_{\text{Alkenes}+\text{O}_3}^i[\text{Alkenes}][\text{O}_3]\} + (k_{\text{O}_3+\text{OH}}[\text{OH}] +  
466 \quad k_{\text{O}_3+\text{HO}_2}[\text{HO}_2])[\text{O}_3] + k_{\text{OH}+\text{NO}_2}[\text{OH}][\text{NO}_2]. \quad (4)$$

467 The net formation rate (P(Ox)) can be calculated by subtracting D(Ox) from F(Ox):

$$468 \quad P(O_x) = F(O_x) - D(O_x). \quad (5)$$

469 The simulated  $\text{RO}_2$  radical concentration was introduced into the F(Ox)  
470 calculation. The diurnal variations in the ozone generation in the different air masses  
471 are shown in Fig. 9. The contribution of the  $\text{HO}_2$  radical to F(Ox) was approximately  
472 60%. The  $\text{RO}_2$  radicals consisted of various types such as methyl peroxy ( $\text{MO}_2$ ),  
473 acetyl peroxy radicals ( $\text{ACO}_3/\text{RCO}_3$ ), and other radicals derived from alkanes  
474 (ALKAP), alkenes (ALKEP), and isoprene (ISOP), which accounted for an additional  
475 40% of the F(Ox). On a daytime basis, the maximum F(Ox) reached 7.4 ppb/h at  
476 around 12:00 in the OCM period, while a persistent-high value (maximum of 12.5  
477 ppb/h at 10:00–14:00) occurred in the LAM period. A vast amount of Ox was  
478 consumed in the nitric acid ( $\text{OH} + \text{NO}_2$ ) formation pathways, i.e., higher than the  
479 ozonolysis removal. The daily averaged ozone production rates were 5.52 and 2.76  
480 ppb/h during the LAM and OCM periods, respectively.



481

482

483

**Fig. 9.** The diurnal profiles of the speciation  $F(O_x)$  and  $D(O_x)$  during Land mass and Ocean mass episodes. The data were calculated by the measured OH and HO<sub>2</sub> and modelled RO<sub>2</sub> radicals.

484

### 4.3 Relationship between precursors and oxidation rates

485

486

487

488

489

490

491

492

493

494

495

496

497

498

499

500

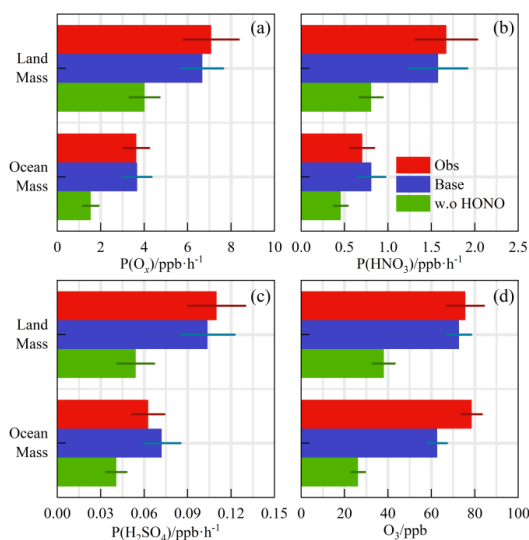
501

502

Despite the low level of human activities, oxidation precursors have an extended lifetime in the stable atmosphere of coastal areas. Intensive photochemical reactions occur after the accumulation of precursors, resulting in local net ozone production comparable to that in the surrounding suburban environments (Zeren et al., 2022). Simultaneous observations of both urban and coastal settings in Shenzhen have indicated that the oxidation rates are comparable (Xia et al., 2021). The coupling of precursor transport and local photochemical processes in marine areas makes it meaningful to explore secondary pollution generation (Fig. 10(a), (b), and (c)). No obvious radical source was missing during the LAM and OCM periods, and the oxidation level was that expected from the base model. On a daytime basis, the mean diurnal profile of the  $P(O_x)$  reached  $\sim 7$  ppb/h in the LAM period, and the average nitric acid ( $P(HNO_3)$ ) and sulfuric acid ( $P(H_2SO_4)$ ) production rates were  $\sim 1.6$  and  $\sim 0.11$  ppb/h, respectively. The  $P(HNO_3)$  production rate was similar to the average of observations in the Pearl River Delta region ( $\sim 1.3$  ppb/h), while that of the  $P(H_2SO_4)$  was only half the average level ( $\sim 0.24$  ppb/h) (Lu et al., 2013; Tan et al., 2019b; Yang et al., 2022b). During the OCM period, the characteristics of the ocean air mass alleviated the photochemical process, and the production rates of the secondary pollutants decreased by approximately half and were close to the average levels in



503 winter (Ma et al., 2019).



504

505

506

507

508

**Fig. 10.** The calculated reaction rates based on the observed concentrations for Land mass and Ocean mass episodes (a) P(O<sub>x</sub>), (b) P(HNO<sub>3</sub>), (c) P(H<sub>2</sub>SO<sub>4</sub>). (d) The observed and modelled O<sub>3</sub> concentration with a first-order loss term. The deposition process was equivalent to a lifetime of 15 hours to all species. All the rates and concentration are averaged for the daytime period between 10:00 and 15:00.

509

510

511

512

513

514

515

516

517

518

519

520

521

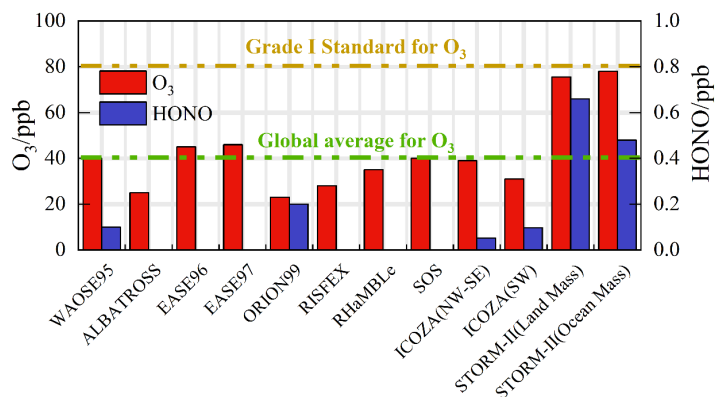
522

523

Contrary to numerous ocean observations, in the YMK site, intensive oxidation was accompanied by a high diurnal HONO level (higher than 400 ppt) (Fig. 11). The ozone levels were consistent with the Grade I air quality standard and far exceeded the global background concentration (~40 ppb). Daytime photolysis reactions of HONO contributed 1.52 ppb/h and 2.19 ppb/h to P(RO<sub>x</sub>) during the OCM and LAM periods, respectively, which were much higher than the values in several megacities during the photochemically polluted season (Tan et al., 2019a). Given the significance of HONO photolysis in driving atmospheric chemistry, a sensitivity test was conducted without constraints on HONO (i.e., w.o HONO) to specifically quantify the contribution of HONO-induced secondary pollution. Only the homogeneous reaction (OH + NO) participated in the formation of HONO in the default mode without HONO input (Liu et al., 2022b). After evaluation, the P(O<sub>x</sub>) was found to be 33% and 39% lower during the LAM and OCM periods, respectively, while the nitric acid and sulfuric acid formation rates were 52% and 35% lower, respectively. The sensitivity test identified the privileged role of the HONO-related mechanisms in the OH



524 chemistry, which resulted in a correlation between the efficient radical recycling and  
 525 secondary pollution.



526

527

528

Fig. 11. Summary of both ozone and HONO concentrations in previous marine observations. The concentrations are averaged for the daytime period between 10:00 and 15:00.

529

A time-dependent box model was used to test the association between the HONO  
 530 chemistry and the local ozone generation (Fig. 10(d)). In order to isolate the the O<sub>3</sub>  
 531 photochemical production, the impacts of vertical entrainment and horizontal  
 532 advection were in general ignored. On the basis of the base scenario run, constraint of  
 533 the observed ozone concentration was removed, and the deposition process was  
 534 equivalent to a lifetime of 15 hours to all species. The observed and modelled O<sub>3</sub>  
 535 concentrations in Fig. 10(d) are averaged for the daytime period between 10:00 and  
 536 15:00. The observed diurnal ozone concentrations were 75.7 ppb and 78.6 ppb during  
 537 the LAM and OCM periods, respectively. The daytime ozone was well reproduced by  
 538 the time-dependent box model, and the deviation of the simulation was less than 20%  
 539 (Fig. 10(d)). After removing the HONO constraint, the simulated ozone  
 540 concentrations were 38.2 and 26.3 ppb, i.e., 48% and 58% lower, during the LAM and  
 541 OCM periods, respectively. Both the HONO and ozone concentrations were reduced  
 542 to a low level (~70 ppt and ~35 ppb) and were close to several ocean observations  
 543 (Fig. 11) (Woodward-Massey et al., 2022b; Zhu et al., 2022; Xia et al., 2022). The  
 544 elevated daytime HONO had an additional effect on the oxidation in the background  
 545 atmosphere. For coastal cities, the particularity of the HONO chemistry in the MBL  
 546 tends to influence the ozone-sensitive system and eventually magnifies the ozone  
 547 background. Therefore, the promotion of oxidation by elevated precursor



548 concentrations is worth considering when formulating emission reduction policies.

## 549 **5 Conclusions**

550 Comprehensive observations of HO<sub>x</sub> radicals and other relevant species were  
551 conducted in October 2019 at a coastal site in the Pearl River Delta (the YMK site,  
552 22.55°N, 114.60°E). The overall air pollutants exhibited typical coastal features due to  
553 the scarce anthropogenic emissions. The average daily maximum OH and HO<sub>2</sub>  
554 concentrations were  $(4.7\text{--}9.5) \times 10^6 \text{ cm}^{-3}$  and  $(4.2\text{--}8.1) \times 10^8 \text{ cm}^{-3}$ , respectively. The  
555 base RACM2-LIM1 model satisfactorily reproduced both the observed OH and HO<sub>2</sub>  
556 radical concentrations, but a slight overestimation of the OH radical occurred. The  
557 daily maximum calculated total OH reactivity was  $9.9 \text{ s}^{-1}$ , and nearly 70% of the  
558 reactivity was contributed by organic species.

559 In addition to anthropogenic and vegetation emissions, the synchronized air mass  
560 transport from the northern cities and the South China Sea exerted a time-varying  
561 influence on radical photochemistry and atmospheric oxidation. During the OCM  
562 period, the observed OH and HO<sub>2</sub> radical concentrations could be reflected by the  
563 base chemical mechanism, with daily average values of  $4.5 \times 10^6 \text{ cm}^{-3}$  and  $4.9 \times 10^8$   
564  $\text{cm}^{-3}$ , respectively. The more active photochemical process during the LAM period  
565 promoted the underestimation of the radical concentrations. Unmeasured reactive  
566 species involved in oxidation propagation were responsible for elevated  
567 photochemistry.

568 In the episode that was dominated by ocean mass, the HO<sub>2</sub> + NO reaction  
569 accounted for ~50% of the primary OH yield. A higher OH generation rate was  
570 found ( $12.6 \text{ ppb/h}$ ) during the LAM period, and the secondary source accounted for 67%  
571 of the total, which was similar to several observations in polluted plumes. Reactions  
572 between RO<sub>x</sub> and NO<sub>x</sub> and self-combination were the main pathways of radical  
573 termination (~70%), and the contribution of peroxyxynitrite formation to the L(RO<sub>x</sub>)  
574 could not be ignored in the daytime.

575 Intensive photochemical reactions occur after the accumulation of precursors,





576 resulting in local net ozone production comparable to that in the surrounding suburban  
577 environments. The daily average ozone production rates were 5.52 and 2.76 ppb/h in  
578 the LAM and OCM periods, respectively. The rapid oxidation process was  
579 accompanied by a higher diurnal HONO concentration (higher than 400 ppt). A non-  
580 HONO-constrained sensitivity test was performed to quantify the HONO-induced  
581 contribution to secondary pollution. After evaluation, the P(Ox) values were 33% and  
582 39% lower during the LAM and OCM periods, respectively, while the nitric acid and  
583 sulfuric acid formation rates were 52% and 35% lower, respectively. The simulated  
584 daytime HONO and ozone concentrations were reduced to a low level (~70 ppt and  
585 ~35 ppb, respectively). For coastal cities, the particularity of the HONO chemistry in  
586 the MBL tends to influence the ozone-sensitive system and eventually magnifies the  
587 ozone background. Therefore, the promotion of oxidation by elevated precursor  
588 concentrations is worth considering when formulating emission reduction policies.

## 589 **Financial support**

590 This work was supported by the National Natural Science Foundation of China  
591 (62275250, U19A2044, 61905003), the Natural Science Foundation of Anhui  
592 Province (No. 2008085J20), the National Key R&D Program of China  
593 (2022YFC3700301), and the Anhui Provincial Key R&D Program (2022107020022).

## 594 **Data availability**

595 The data used in this study are available from the corresponding author upon request  
596 (rzhu@aiofm.ac.cn).

## 597 **Author contributions**

598 WQ Liu, PH Xie, RZ Hu contributed to the conception of this study. GX Zhang and  
599 RZ Hu performed the data analyses and manuscript writing. All authors contributed to  
600 measurements, discussed results, and commented on the paper.



601 **Competing interests**

602 The contact author has declared that none of the authors has any competing interests.

603

604



## 605 **References**

- 606 Brauers, T., Hausmann, M., Bister, A., Kraus, A., and Dorn, H.-P.: OH radicals in the boundary layer of  
607 the Atlantic Ocean: 1. Measurements by long-path laser absorption spectroscopy, *Journal of*  
608 *Geophysical Research*, 106, 7399, 10.1029/2000jd900679, 2001.
- 609 Carpenter, L. J., Fleming, Z. L., Read, K. A., Lee, J. D., Moller, S. J., Hopkins, J. R., Purvis, R. M.,  
610 Lewis, A. C., Müller, K., Heinold, B., Herrmann, H., Fomba, K. W., van Pinxteren, D., Müller, C.,  
611 Tegen, I., Wiedensohler, A., Müller, T., Niedermeier, N., Achterberg, E. P., Patey, M. D., Kozlova, E. A.,  
612 Heimann, M., Heard, D. E., Plane, J. M. C., Mahajan, A., Oetjen, H., Ingham, T., Stone, D., Whalley, L.  
613 K., Evans, M. J., Pilling, M. J., Leigh, R. J., Monks, P. S., Karunaharan, A., Vaughan, S., Arnold, S. R.,  
614 Tschritter, J., Pöhler, D., Frieb, U., Holla, R., Mendes, L. M., Lopez, H., Faria, B., Manning, A. J., and  
615 Wallace, D. W. R.: Seasonal characteristics of tropical marine boundary layer air measured at the Cape  
616 Verde Atmospheric Observatory, *J Atmos Chem*, 67, 87-140, 10.1007/s10874-011-9206-1, 2011.
- 617 Carslaw, N., Creasey, D. J., Heard, D. E., Lewis, A. C., McQuaid, J. B., Pilling, M. J., Monks, P. S.,  
618 Bandy, B. J., and Penkett, S. A.: Modeling OH, HO<sub>2</sub>, and RO<sub>2</sub>radicals in the marine boundary layer: 1.  
619 Model construction and comparison with field measurements, *Journal of Geophysical Research:*  
620 *Atmospheres*, 104, 30241-30255, 10.1029/1999jd900783, 1999.
- 621 Chen, W., Guenther, A. B., Shao, M., Yuan, B., Jia, S., Mao, J., Yan, F., Krishnan, P., and Wang, X.:  
622 Assessment of background ozone concentrations in China and implications for using region-specific  
623 volatile organic compounds emission abatement to mitigate air pollution, *Environ Pollut*, 305, 119254,  
624 10.1016/j.envpol.2022.119254, 2022.
- 625 Creasey, D. J., Heard, D. E., and Lee, J. D.: Eastern Atlantic Spring Experiment 1997 (EASE97) 1.  
626 Measurements of OH and HO<sub>2</sub> concentrations at Mace Head, Ireland, *Journal of Geophysical Research:*  
627 *Atmospheres*, 107, ACH 3-1-ACH 3-15, 10.1029/2001jd000892, 2002.
- 628 Crilley, L. R., Kramer, L. J., Pope, F. D., Reed, C., Lee, J. D., Carpenter, L. J., Hollis, L. D. J., Ball, S.  
629 M., and Bloss, W. J.: Is the ocean surface a source of nitrous acid (HONO) in the marine boundary  
630 layer?, *Atmos Chem Phys*, 21, 18213-18225, 10.5194/acp-21-18213-2021, 2021.
- 631 Fuchs, H., Dorn, H. P., Bachner, M., Bohn, B., Brauers, T., Gomm, S., Hofzumahaus, A., Holland, F.,  
632 Nehr, S., Rohrer, F., Tillmann, R., and Wahner, A.: Comparison of OH concentration measurements by  
633 DOAS and LIF during SAPHIR chamber experiments at high OH reactivity and low NO concentration,  
634 *Atmos Meas Tech*, 5, 1611-1626, 10.5194/amt-5-1611-2012, 2012.
- 635 Fuchs, H., Tan, Z., Lu, K., Bohn, B., Broch, S., Brown, S. S., Dong, H., Gomm, S., Haeseler, R., He, L.,  
636 Hofzumahaus, A., Holland, F., Li, X., Liu, Y., Lu, S., Min, K.-E., Rohrer, F., Shao, M., Wang, B., Wang,  
637 M., Wu, Y., Zeng, L., Zhang, Y., Wahner, A., and Zhang, Y.: OH reactivity at a rural site (Wangdu) in  
638 the North China Plain: contributions from OH reactants and experimental OH budget, *Atmos Chem*  
639 *Phys*, 17, 645-661, 10.5194/acp-17-645-2017, 2017.
- 640 Grenfell, J. L., Savage, N. H., Harrison, R. M., Penkett, S. A., Forberich, O., Comes, F. J., Clemshaw,  
641 K. C., Burgess, R. A., Cardenas, L. M., Davison, B., and McFadyen, G. G.: Tropospheric box-  
642 modelling and analytical studies of the hydroxyl (OH) radical and related species: Comparison with  
643 observations, *J Atmos Chem*, 33, 183-214, 10.1023/a:1006009901180, 1999.
- 644 Griffith, S. M., Hansen, R. F., Dusanter, S., Stevens, P. S., Alaghmand, M., Bertman, S. B., Carroll, M.  
645 A., Erickson, M., Galloway, M., Grossberg, N., Hottle, J., Hou, J., Jobson, B. T., Kamrath, A.,  
646 Keutsch, F. N., Lefer, B. L., Mielke, L. H., O'Brien, A., Shepson, P. B., Thurlow, M., Wallace, W.,



- 647 Zhang, N., and Zhou, X. L.: OH and HO<sub>2</sub> radical chemistry during PROPHET 2008 and CABINEX  
648 2009-Part 1: Measurements and model comparison, *Atmos Chem Phys*, 13, 5403-5423, 10.5194/acp-  
649 13-5403-2013, 2013.
- 650 Hofzumahaus, A., Rohrer, F., Lu, K., Bohn, B., Brauers, T., Chang, C.-C., Fuchs, H., Holland, F., Kita,  
651 K., Kondo, Y., Li, X., Lou, S., Shao, M., Zeng, L., Wahner, A., and Zhang, Y.: Amplified Trace Gas  
652 Removal in the Troposphere, *Science*, 324, 1702-1704, 10.1126/science.1164566, 2009.
- 653 Huang, R. J., Hoffmann, T., Ovadnevaite, J., Laaksonen, A., Kokkola, H., Xu, W., Xu, W., Ceburnis, D.,  
654 Zhang, R., Seinfeld, J. H., and O'Dowd, C.: Heterogeneous iodine-organic chemistry fast-tracks marine  
655 new particle formation, *Proc Natl Acad Sci U S A*, 119, e2201729119, 10.1073/pnas.2201729119, 2022.
- 656 Jiang, Y., Xue, L., Shen, H., Dong, C., Xiao, Z., and Wang, W.: Dominant Processes of HONO Derived  
657 from Multiple Field Observations in Contrasting Environments, *Environmental Science & Technology*  
658 *Letters*, 10.1021/acs.estlett.2c00004, 2022.
- 659 Kanaya, Y., Sadanaga, Y., Nakamura, K., and Akimoto, H.: Behavior of OH and HO<sub>2</sub> radicals during  
660 the Observations at a Remote Island of Okinawa (ORION99) field campaign 1. Observation using a  
661 laser-induced fluorescence instrument, *J Geophys Res-Atmos*, 106, 24197-24208,  
662 10.1029/2000jd000178, 2001.
- 663 Kanaya, Y., Yokouchi, Y., Matsumoto, J., Nakamura, K., Kato, S., Tanimoto, H., Furutani, H., Toyota,  
664 K., and Akimoto, H.: Implications of iodine chemistry for daytime HO<sub>2</sub> levels at Rishiri Island,  
665 *Geophys Res Lett*, 29, 45-41-45-44, 10.1029/2001gl014061, 2002.
- 666 Liu, C., Liu, G., Casazza, M., Yan, N., Xu, L., Hao, Y., Franzese, P. P., and Yang, Z.: Current Status and  
667 Potential Assessment of China's Ocean Carbon Sinks, *Environ Sci Technol*, 56, 6584-6595,  
668 10.1021/acs.est.1c08106, 2022a.
- 669 Liu, P., Xue, C., Ye, C., Liu, C., Zhang, C., Wang, J., Zhang, Y., Liu, J., and Mu, Y.: The Lack of  
670 HONO Measurement May Affect the Accurate Diagnosis of Ozone Production Sensitivity, *ACS*  
671 *Environmental Au*, 10.1021/acsenvironau.2c00048, 2022b.
- 672 Liu, T., Hong, Y., Li, M., Xu, L., Chen, J., Bian, Y., Yang, C., Dan, Y., Zhang, Y., Xue, L., Zhao, M.,  
673 Huang, Z., and Wang, H.: Atmospheric oxidation capacity and ozone pollution mechanism in a coastal  
674 city of southeastern China: analysis of a typical photochemical episode by an observation-based model,  
675 *Atmos Chem Phys*, 22, 2173-2190, 10.5194/acp-22-2173-2022, 2022c.
- 676 Lou, S., Holland, F., Rohrer, F., Lu, K., Bohn, B., Brauers, T., Chang, C. C., Fuchs, H., Haseler, R.,  
677 Kita, K., Kondo, Y., Li, X., Shao, M., Zeng, L., Wahner, A., Zhang, Y., Wang, W., and Hofzumahaus, A.:  
678 Atmospheric OH reactivities in the Pearl River Delta – China in summer 2006: measurement and  
679 model results, *Atmos Chem Phys*, 10, 11243–11260, 10.5194/acp-10-11243-2010, 2010.
- 680 Lu, K. D., Guo, S., Tan, Z. F., Wang, H. C., Shang, D. J., Liu, Y. H., Li, X., Wu, Z. J., Hu, M., and  
681 Zhang, Y. H.: Exploring atmospheric free-radical chemistry in China: the self-cleansing capacity and  
682 the formation of secondary air pollution, *Natl. Sci. Rev.*, 6, 579-594, 10.1093/nsr/nwy073, 2019.
- 683 Lu, K. D., Hofzumahaus, A., Holland, F., Bohn, B., Brauers, T., Fuchs, H., Hu, M., Haeseler, R., Kita,  
684 K., Kondo, Y., Li, X., Lou, S. R., Oebel, A., Shao, M., Zeng, L. M., Wahner, A., Zhu, T., Zhang, Y. H.,  
685 and Rohrer, F.: Missing OH source in a suburban environment near Beijing: observed and modelled  
686 OH and HO<sub>2</sub> concentrations in summer 2006, *Atmos Chem Phys*, 13, 1057-1080, 10.5194/acp-13-  
687 1057-2013, 2013.
- 688 Lu, K. D., Rohrer, F., Holland, F., Fuchs, H., Bohn, B., Brauers, T., Chang, C. C., Haeseler, R., Hu, M.,  
689 Kita, K., Kondo, Y., Li, X., Lou, S. R., Nehr, S., Shao, M., Zeng, L. M., Wahner, A., Zhang, Y. H., and  
690 Hofzumahaus, A.: Observation and modelling of OH and HO<sub>2</sub> concentrations in the Pearl River Delta



- 691 2006: a missing OH source in a VOC rich atmosphere, *Atmos Chem Phys*, 12, 1541-1569,  
692 10.5194/acp-12-1541-2012, 2012.
- 693 Ma, X. F., Tan, Z. F., Lu, K. D., Yang, X. P., Liu, Y. H., Li, S. L., Li, X., Chen, S. Y., Novelli, A., Cho,  
694 C. M., Zeng, L. M., Wahner, A., and Zhang, Y. H.: Winter photochemistry in Beijing: Observation and  
695 model simulation of OH and HO<sub>2</sub> radicals at an urban site, *Sci Total Environ*, 685, 85-95,  
696 10.1016/j.scitotenv.2019.05.329, 2019.
- 697 Mallik, C., Tomsche, L., Boutsoukidis, E., Crowley, J. N., Derstroff, B., Fischer, H., Hafermann, S.,  
698 Hüser, I., Javed, U., Keßel, S., Lelieveld, J., Martinez, M., Meusel, H., Novelli, A., Phillips, G. J.,  
699 Pozzer, A., Reiffs, A., Sander, R., Taraborrelli, D., Sauvage, C., Schuladen, J., Su, H., Williams, J., and  
700 Harder, H.: Oxidation processes in the eastern Mediterranean atmosphere: evidence from the modelling  
701 of HO<sub>2</sub> and measurements over Cyprus, *Atmos Chem Phys*, 18,  
702 10825-10847, 10.5194/acp-18-10825-2018, 2018.
- 703 Niu, Y. B., Zhu, B., He, L. Y., Wang, Z., Lin, X. Y., Tang, M. X., and Huang, X. F.: Fast Nocturnal  
704 Heterogeneous Chemistry in a Coastal Background Atmosphere and Its Implications for Daytime  
705 Photochemistry, *Journal of Geophysical Research: Atmospheres*, 127, 10.1029/2022jd036716, 2022.
- 706 Peng, X., Wang, W. H., Xia, M., Chen, H., Ravishankara, A. R., Li, Q. Y., Saiz-Lopez, A., Liu, P. F.,  
707 Zhang, F., Zhang, C. L., Xue, L. K., Wang, X. F., George, C., Wang, J. H., Mu, Y. J., Chen, J. M., and  
708 Wang, T.: An unexpected large continental source of reactive bromine and chlorine with significant  
709 impact on wintertime air quality, *Natl. Sci. Rev.*, 8, 10.1093/nsr/nwaa304, 2021.
- 710 Qi, B., Kanaya, Y., Takami, A., Hatakeyama, S., Kato, S., Sadanaga, Y., Tanimoto, H., and Kajii, Y.:  
711 Diurnal peroxy radical chemistry at a remote coastal site over the sea of Japan, *Journal of Geophysical*  
712 *Research*, 112, 10.1029/2006jd008236, 2007.
- 713 Stockwell, W. R., Kirchner, F., Kuhn, M., and Seefeld, S.: A new mechanism for regional atmospheric  
714 chemistry modeling, *J Geophys Res-Atmos*, 102, 25847-25879, 10.1029/97jd00849, 1997.
- 715 Stone, D., Whalley, L. K., and Heard, D. E.: Tropospheric OH and HO<sub>2</sub> radicals: field measurements  
716 and model comparisons, *Chemical Society reviews*, 41, 6348-6404, 10.1039/c2cs35140d, 2012.
- 717 Sun, L., Chen, T., Jiang, Y., Zhou, Y., Sheng, L., Lin, J., Li, J., Dong, C., Wang, C., Wang, X., Zhang,  
718 Q., Wang, W., and Xue, L.: Ship emission of nitrous acid (HONO) and its impacts on the marine  
719 atmospheric oxidation chemistry, *Sci Total Environ*, 735, 139355, 10.1016/j.scitotenv.2020.139355,  
720 2020.
- 721 Tan, Z., Lu, K., Ma, X., Chen, S., He, L., Huang, X., Li, X., Lin, X., Tang, M., Yu, D., Wahner, A., and  
722 Zhang, Y.: Multiple Impacts of Aerosols on O(3) Production Are Largely Compensated: A Case Study  
723 Shenzhen, China, *Environ Sci Technol*, 10.1021/acs.est.2c06217, 2022.
- 724 Tan, Z., Lu, K., Jiang, M., Su, R., Wang, H., Lou, S., Fu, Q., Zhai, C., Tan, Q., Yue, D., Chen, D., Wang,  
725 Z., Xie, S., Zeng, L., and Zhang, Y.: Daytime atmospheric oxidation capacity in four Chinese  
726 megacities during the photochemically polluted season: a case study based on box model simulation,  
727 *Atmos Chem Phys*, 19, 3493-3513, 10.5194/acp-19-3493-2019, 2019a.
- 728 Tan, Z. F., Lu, K. D., Hofzumahaus, A., Fuchs, H., Bohn, B., Holland, F., Liu, Y. H., Rohrer, F., Shao,  
729 M., Sun, K., Wu, Y. S., Zeng, L. M., Zhang, Y. S., Zou, Q., Kiendler-Scharr, A., Wahner, A., and Zhang,  
730 Y. H.: Experimental budgets of OH, HO<sub>2</sub>, and RO<sub>2</sub> radicals and implications for ozone formation in  
731 the Pearl River Delta in China 2014, *Atmos Chem Phys*, 19, 7129-7150, 10.5194/acp-19-7129-2019,  
732 2019b.
- 733 Tan, Z. F., Fuchs, H., Lu, K. D., Hofzumahaus, A., Bohn, B., Broch, S., Dong, H. B., Gomm, S.,  
734 Haseler, R., He, L. Y., Holland, F., Li, X., Liu, Y., Lu, S. H., Rohrer, F., Shao, M., Wang, B. L., Wang,



- 735 M., Wu, Y. S., Zeng, L. M., Zhang, Y. S., Wahner, A., and Zhang, Y. H.: Radical chemistry at a rural  
736 site (Wangdu) in the North China Plain: observation and model calculations of OH, HO<sub>2</sub> and RO<sub>2</sub>  
737 radicals, *Atmos Chem Phys*, 17, 663-690, 10.5194/acp-17-663-2017, 2017.
- 738 Vaughan, S., Ingham, T., K. Whalley, L., Stone, D., Evans, M. J., Read, K. A., Lee, J. D., Moller, S. J.,  
739 Carpenter, L. J., Lewis, A. C., Fleming, Z. L., and Heard, D. E.: Seasonal observations of OH and HO<sub>2</sub>  
740 in the remote tropical marine boundary layer, *Atmos. Chem. Phys.*, 12, 2149–2172, 10.5194/acp-12-  
741 2149-2012, 2012.
- 742 Wang, F., Hu, R., Xie, P., Wang, Y., Chen, H., Zhang, G., and Liu, W.: Calibration source for OH  
743 radical based on synchronous photolysis, *Acta Phys Sin-Ch Ed*, 69, 2020.
- 744 Wang, F. Y., Hu, R. Z., Chen, H., Xie, P. H., Wang, Y. H., Li, Z. Y., Jin, H. W., Liu, J. G., and Liu, W. Q.:  
745 Development of a field system for measurement of tropospheric OH radical using laser-induced  
746 fluorescence technique, *Opt. Express*, 27, A419-A435, 10.1364/oe.27.00a419, 2019.
- 747 Wang, T., Wei, X. L., Ding, A. J., Poon, C. N., Lam, K. S., Li, Y. S., Chan, L. Y., and Anson, M.:  
748 Increasing surface ozone concentrations in the background atmosphere of Southern China, 1994-2007,  
749 *Atmos Chem Phys*, 9, 6217-6227, 10.5194/acp-9-6217-2009, 2009.
- 750 Wang, Y., Hu, R., Xie, P., Chen, H., Wang, F., Liu, X., Liu, J., and Liu, W.: Measurement of  
751 tropospheric HO<sub>2</sub> radical using fluorescence assay by gas expansion with low interferences, *J Environ*  
752 *Sci (China)*, 99, 40-50, 10.1016/j.jes.2020.06.010, 2021.
- 753 Whalley, L. K., Furneaux, K. L., Goddard, A., Lee, J. D., Mahajan, A., Oetjen, H., Read, K. A., Kaaden,  
754 N., Carpenter, L. J., Lewis, A. C., Plane, J. M. C., Saltzman, E. S., Wiedensohler, A., and Heard, D. E.:  
755 The chemistry of OH and HO<sub>2</sub> radicals in the boundary layer over the tropical Atlantic Ocean, *Atmos*  
756 *Chem Phys*, 10, 1555-1576, 2010.
- 757 Woodward-Massey, R., Sommariva, R., Whalley, L. K., Cryer, D. R., Ingham, T., Bloss, W. J., Ball, S.  
758 M., Lee, J. D., Reed, C. P., Crilley, L. R., Kramer, L. J., Bandy, B. J., Forster, G. L., Reeves, C. E.,  
759 Monks, P. S., and Heard, D. E.: Radical chemistry at a UK coastal receptor site – Part 2: experimental  
760 radical budgets and ozone production, *Atmos. Chem. Phys.*, 10.5194/acp-2022-213, 2022a.
- 761 Woodward-Massey, R., Sommariva, R., Whalley, L. K., Cryer, D. R., Ingham, T., Bloss, W. J., Ball, S.  
762 M., Lee, J. D., Reed, C. P., Crilley, L. R., Kramer, L. J., Bandy, B. J., Forster, G. L., Reeves, C. E.,  
763 Monks, P. S., and Heard, D. E.: Radical chemistry at a UK coastal receptor site – Part 1: observations  
764 of OH, HO<sub>2</sub>, RO<sub>2</sub>, and OH reactivity and comparison to MCM model predictions, *Atmos. Chem. Phys.*,  
765 10.5194/acp-2022-207, 2022b.
- 766 Xia, M., Wang, T., Wang, Z., Chen, Y., Peng, X., Huo, Y., Wang, W., Yuan, Q., Jiang, Y., Guo, H., Lau,  
767 C., Leung, K., Yu, A., and Lee, S.: Pollution-Derived Br<sub>2</sub> Boosts Oxidation Power of the Coastal  
768 Atmosphere, *Environ Sci Technol*, 10.1021/acs.est.2c02434, 2022.
- 769 Xia, S.-Y., Zhu, B., Wang, S.-X., Huang, X.-F., and He, L.-Y.: Spatial distribution and source  
770 apportionment of peroxyacetyl nitrate (PAN) in a coastal region in southern China, *Atmos Environ*, 260,  
771 10.1016/j.atmosenv.2021.118553, 2021.
- 772 Xu, W., Ovadnevaite, J., Fossum, K. N., Lin, C., Huang, R.-J., Ceburnis, D., and O’Dowd, C.: Sea  
773 spray as an obscured source for marine cloud nuclei, *Nature Geoscience*, 15, 282-286, 10.1038/s41561-  
774 022-00917-2, 2022.
- 775 Yang, X., Lu, K., Ma, X., Gao, Y., Tan, Z., Wang, H., Chen, X., Li, X., Huang, X., He, L., Tang, M.,  
776 Zhu, B., Chen, S., Dong, H., Zeng, L., and Zhang, Y.: Radical chemistry in the Pearl River Delta:  
777 observations and modeling of OH and HO<sub>2</sub> radicals in Shenzhen in 2018, *Atmos Chem Phys*, 22,  
778 12525-12542, 10.5194/acp-22-12525-2022, 2022a.



779 Yang, X., Lu, K., Ma, X., Gao, Y., Tan, Z., Wang, H., Chen, X., Li, X., Huang, X., He, L., Tang, M.,  
780 Zhu, B., Chen, S., Dong, H., Zeng, L., and Zhang, Y.: Radical chemistry in the Pearl River Delta:  
781 observations and 2 modeling of OH and HO<sub>2</sub> radicals in Shenzhen 2018, 10.5194/acp-2022-113, 2022b.  
782 Yang, X., Lu, K., Ma, X., Liu, Y., Wang, H., Hu, R., Li, X., Lou, S., Chen, S., Dong, H., Wang, F.,  
783 Wang, Y., Zhang, G., Li, S., Yang, S., Yang, Y., Kuang, C., Tan, Z., Chen, X., Qiu, P., Zeng, L., Xie, P.,  
784 and Zhang, Y.: Observations and modeling of OH and HO<sub>2</sub> radicals in Chengdu, China in summer  
785 2019, *The Science of the total environment*, 772, 144829-144829, 10.1016/j.scitotenv.2020.144829,  
786 2021.  
787 Zeren, Y., Zhou, B., Zheng, Y., Jiang, F., Lyu, X., Xue, L., Wang, H., Liu, X., and Guo, H.: Does Ozone  
788 Pollution Share the Same Formation Mechanisms in the Bay Areas of China?, *Environ Sci Technol*,  
789 10.1021/acs.est.2c05126, 2022.  
790 Zhang, G., Hu, R., Xie, P., Lou, S., Wang, F., Wang, Y., Qin, M., Li, X., Liu, X., Wang, Y., and Liu, W.:  
791 Observation and simulation of HO<sub>x</sub> radicals in an urban area in Shanghai, China, *Sci Total Environ*,  
792 810, 152275, 10.1016/j.scitotenv.2021.152275, 2022a.  
793 Zhang, G., Hu, R., Xie, P., Lu, K., Lou, S., Liu, X., Li, X., Wang, F., Wang, Y., Yang, X., Cai, H., Wang,  
794 Y., and Liu, W.: Intercomparison of OH radical measurement in a complex atmosphere in Chengdu,  
795 China, *Sci Total Environ*, 155924, 10.1016/j.scitotenv.2022.155924, 2022b.  
796 Zhu, Y., Wang, Y., Zhou, X., Elshorbany, Y. F., Ye, C., Hayden, M., and Peters, A. J.: An investigation  
797 into the chemistry of HONO in the marine boundary layer at Tudor Hill Marine Atmospheric  
798 Observatory in Bermuda, *Atmos Chem Phys*, 22, 6327-6346, 10.5194/acp-22-6327-2022, 2022.  
799 Zou, Z., Chen, Q., Xia, M., Yuan, Q., Chen, Y., Wang, Y., Xiong, E., Wang, Z., and Wang, T.: OH  
800 measurements in the coastal atmosphere of South China: missing OH sinks in aged air masses,  
801 *EGUsphere*, 2022, 1-47, 10.5194/egusphere-2022-854, 2022.  
802